Linking plastic heterogeneity of bulk metallic glasses to quench-in structural defects with machine learning

Qi Wang, Anubhav Jain

Lawrence Berkeley National Laboratory, Energy Technologies Area,

1 Cyclotron Road, Berkeley, CA 94720

ABSTRACT

When metallic glasses are subjected to mechanical loads, the plastic response of atoms is heterogeneous. However, the degree to which the plastic units are correlated with the structural defects frozen in the quenched glass structure is still elusive. Here, we introduce a machine learning framework to predict the plastic heterogeneity of atoms in Cu-Zr metallic glasses solely from the undeformed, quenched configuration. We propose that an atomic-scale quantity, "quench-in softness", calibrated from a gradient boosted decision tree model trained on a set of short- and medium-range site features, can identify plastically susceptible sites at various strain levels with high accuracy. The predictive ability is further confirmed in that a model trained on a single composition and quench rate retains high accuracy on other compositions and quench rates without any further training. We also quantitatively assess historical site descriptors against our method, demonstrating that the regularity-related features introduced in this work are more predictive and may play an important role in future glass characterization. Our work presents a general, data-centric framework that could potentially be used to address the structural origin of any site-specific property in metallic glasses.

1. Introduction

Disordered solids are ubiquitous in nature and technology¹, encompassing colloids², granular particles³, hard-sphere glasses⁴ and amorphous silicon⁵. Metallic glasses⁶, especially bulk metallic glasses^{7,8}, are a relatively new member of this family. The combination of "metal" and "glass" not only produces many technologically useful properties such as ultrahigh strength, thermoplastic formability and corrosion resistance, but also introduces many unique and incompletely understood fundamental issues⁹.

Understanding and controlling deformation is a long-standing issue in metallic glasses^{10–12}. Unlike in crystals, in a disordered material every atom has a unique atomic environment and so the response of every atom to the macroscopic loading conditions can, in principle, be different. This difference leads to localized plastic flow, even in the elastic stage, confined to regions called shear transformation zones.^{13–15} This shear mechanism differs strikingly from the dislocation-mediated plasticity in crystals and can also be found in many geological hazards, such as debris flows, avalanches, landslides and earthquakes⁸.

The central paradigm of materials science states that structure and mechanical property are interrelated. However, such connections between the highly heterogeneous atomic-scale structure and mechanical response are challenging for metallic glasses. In particular, a fundamental issue that this work aims to address is the degree to which plastic regions are simply defects frozen in the initial glass structure (and can be identified prior to loading) versus events that are stochastic under the loading protocol. This is still in hot debate and addressing this puzzle is crucial to the long-term goal of realizing the inverse control of metallic glass deformation^{16,17}. Quantitative insights on what structural signatures are the most important and how they would influence the plastic susceptibility of atoms are also lacking⁹.

Here, we seek to use a combination of simulations and machine learning 18-25 (ML) to

develop a model that can predict plastic regions in Cu-Zr metallic glasses, even at high levels of strain, based on the initial structural data (i.e., atomic positions) alone. This task differs from the pioneering works by Cubuk et al^{24,25} in that (i) only the initial configuration is used as an input (as opposed to step-by-step snapshots within shorter strain intervals), (ii) a comprehensive set of recognized and newly designed short- and medium-range descriptors are used (as opposed to symmetry functions), and (iii) Cu-Zr metallic glasses with a more realistic and many-body interaction are studied (as opposed to Lennard-Jones pair-potential that lacks environmental dependence²⁶). In addition, as the glass property is heavily dependent on the composition and processing protocols, we also address the significant yet unsettled question of whether a ML model trained under a single condition can generalize well to other compositions and processing protocols. Furthermore, we use ML as an effective tool to identify the site characteristics that distinguish regions susceptible to plastic deformation from those that are relatively stable. This work can pave a data-centric way towards rapid screening and target control of metallic glass structures with desired deformation characteristics.

In our approach, we build a large representation of 740+ candidate features, including both known and new signatures, to represent the geometry and chemistry at short and medium length scales around each atom. We train a gradient-boosted decision tree model that defines a site-specific quantity, "quench-in softness", that has the potential to predict the long-term plastic response of a metallic glass, prior to performing any simulations. Our results suggest that plastic deformation until the formation of shear bands is to a large degree controlled by the intrinsic structure rather than complex dynamics. We demonstrate that our ML framework is robust and readily generalizable across glasses and quenching conditions, suggesting that the types of sites prone to rearrangement are consistent across different compositions and glass configurations. We also identify a set of new structure

signatures that exceeds the predictive powers of existing signatures that are recognized in this field. This ML framework is general and can be conceivably applied to predict any sitespecific property of metallic glasses for which data is available or can be generated.

2. Results

Predicting plastic atoms a priori in prototypical Cu-Zr metallic glasses. Figure 1 illustrates the design of our ML framework. The procedure involves a "featurization" or "fingerprinting" step in which the site environments of a metallic glass are represented numerically in terms of short- and medium-range orders, followed by a ML mapping between the features and the property of interest, i.e. whether an atom is susceptible to plastic rearrangement or not. In this work, we select Cu-Zr metallic glasses, one of the most popular bulk-metallic-glassforming systems^{27–35}, as prototypical alloys. To generate deformation data for ML, we quench (2000 K to 50 K) and uniaxially compress (50 K) a series of large (345600 atoms) metallic glass samples by molecular dynamics simulations (see Methods). Three independent samples are quenched for each of 3 different compositions of Cu_xZr_{1-x} (x = 50, 65 and 80 at.%) and under 3 quenching rates of 5 \times 10¹⁰, 5 \times 10¹¹ and 5 \times 10¹² Ks⁻¹, resulting in a total of 27 configurations under 9 separate conditions. Two of the 3 samples per condition are used for training, whereas the third sample is set aside for generalization tests and completely unseen during all model development. We analyze plastic heterogeneity of atoms under each strain by calculating non-affine displacement (D^2) as plastic indicator¹⁴ with a threshold of 5.0 Å² to distinguish plastic and non-plastic atoms (see Methods). A schematic picture of the data generation pathway and the compatibility of D^2 with other plastic indicators (e.g., local strain η^{mises}) are included in Supplementary Figures S1 and S2. We will use this data to develop an ML model that, using the uncompressed configuration alone, predicts the atoms that are prone to deform plastically.

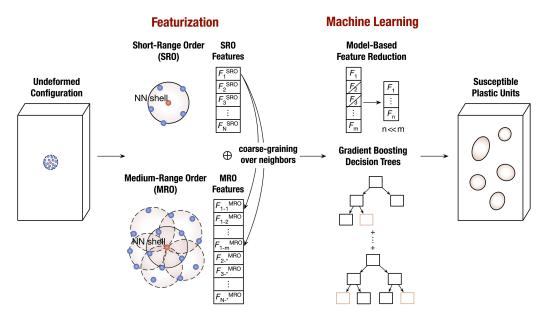


Figure 1 (color online) | Design of the machine learning framework for predicting the heterogeneous, site-specific plastic response of atoms in metallic glasses solely from the undeformed glass configuration. The aim of this work is to locate the possible plastic atoms across a large strain regime from the undeformed configuration using ML. A comprehensive representation consisting of 740+ site features is established for featurizing the short- (SRO) and medium-range order (MRO) around each atom, and MRO features are generated by an automatic neighboring coarse-grained method. Model-based feature reduction is performed to reduce this large set to 13 features. The gradient boosting decision tree (GBDT) algorithm is employed to build the ML model.

Site representation spanning short- and medium-range order. As illustrated in Figure 1, to develop an ML model, we need to develop representations of atoms sites that adequately capture the heterogeneity of site environments in metallic glasses. Previously, researchers in the field of metallic glasses have developed various signatures³⁶⁻⁴⁰ such as coordination number (CN)³⁶, Voronoi indices³⁶, characteristic motifs^{37,38} and *i*-fold symmetry indices³⁹. These features are interpretable yet are highly degenerate and insufficient to distinguish the variety of atomic environments. Concepts of soft modes^{41,42} and flexibility volume⁴³ are more powerful but require knowledge of atomic interactions and cannot be obtained from the glass configuration itself. Recently, function-form features, such as Gaussian symmetry functions²⁰ or bi-spectrum coefficients²³ are also found to be promising representations of atomic information^{24,25}. Nonetheless, the complex transformations involved make it difficult

to interpret the features and models. Furthermore, existing signatures in metallic glasses are mostly targeted for short-range order (SRO), i.e., essentially near neighbors. As we will later demonstrate, medium range order (MRO) features that extend beyond nearest neighbors are required to obtain the most accurate models.

Here, we establish a comprehensive representation that spans SRO and MRO in metallic glasses. Each atom is represented by a set of 746 variables, concatenated from the two families of SRO and MRO features ($F = F^{\text{SRO}} \oplus F^{\text{MRO}}$). For SRO, we use a total of 123 candidate SRO features, divided into 12 distinct groups or "feature sets", as potential inputs for ML models (Table 1, described further in Methods). In addition to the recognized feature sets as mentioned above, we introduce in this work new feature sets by taking statistics (mean, std, max and min) of neighboring distances (or say bond lengths), Voronoi facet areas and sub-polygon volumes around each atom to dig deeper into the local topology. These new features encode more information on the "regularity" or anisotropy in the coordination environments. We will later show that these features are revealed to be more effective than the widely recognized ones in predicting the plastic heterogeneity.

Next, we develop MRO features as few MRO signatures of glass structure are available in literature^{34,44}. To develop MRO features, we generalize a coarse-graining strategy in which statistics of SRO features for a central atom's *neighbors* are used to describe the central atom itself. Specifically, we can process a given SRO feature to calculate the statistics such as sum, mean, std, min or max across the neighbors of each atom i,

$$F_i^{\text{MRO}} = \text{Stats}(F_1^{\text{SRO}}, F_2^{\text{SRO}}, ..., F_n^{\text{SRO}}), \quad n \in \text{NN}(i)$$
 (1)

where n iterates the neighbors NN(i) determined by Voronoi tessellation analysis or within a cutoff distance. This allows automatic encoding of the 2^{nd} neighbor effect, similar to the idea of imposing convolution⁴⁵ over neighbors for feature extraction. Crucially, this strategy allows us to transform any numeric SRO feature into a set of MRO features. As an example,

| Table 1 Short-range order (SRO) feature sets. | | | | |
|---|---|-------|--|--|
| Features | Description | Count | | |
| $CN_{ m Voro/Dist}$ | Number of neighboring atoms determined by Voronoi tessellation analysis ³⁶ or within a cutoff distance. | | | |
| Voronoi idx ₃₇ | $\{n_i\}$ where n_i denotes the number of <i>i</i> -edged facets (<i>i</i> in the range of 3-7) of the Voronoi polyhedra ³⁶ . | | | |
| Characteristic motifs | One-hot encoded signatures of whether a cluster belongs to characteristic motifs e.g. $<0,0,12,0,0>$, $<0,0,12,4,0>$, $<0,0,12,0,0>$ $<0,0,12,4,0>$ or Frank-Kasper-type clusters ³⁷ . | | | |
| Voronoi area/volume | Total facet area and volume of the Voronoi polyhedron around each site. The area and volume are divided by average facet area and sub-polyhedra volume to eliminate system effects. | | | |
| i-fold symm idx ₃₇ | $n_i/\sum_{i=3}^7 n_i$ where n_i is Voronoi index (<i>i</i> in the range of 3-7), reflecting the strength of <i>i</i> -fold symmetry in local sites ³⁹ . | | | |
| Weighted i -fold symm idx_{37} | Weighted i -fold symmetry indices using Voronoi facet areas. | 10 | | |
| BOOP $q_{410\text{-Voro/Dist}}$ | Lowest-order rotation-invariant q_l ($l=4, 6, 8$ and 10) of the l th moment in a multipole expansion of the bond vector distribution on a unit sphere ⁴⁰ . | 8 | | |
| BOOP $w_{410\text{-Voro/Dist}}$ | Higher-order rotation-invariant w_l ($l = 4, 6, 8$ and 10) 40. | 8 | | |
| $CSRO_{Voro/Dist} \\$ | Element type, the number and partial composition of each element in the neighboring shell as well as the deviation of local chemistry with nominal composition (Warren-Cowley parameters ^{46,47}). | 13 | | |
| Facet area stats | Area statistics (mean, std, min and max) of Voronoi facets, and independent statistics (mean, std, min, max and sum) for i -edged facets. | 29 | | |
| Sub-polyhedra volume stats | Volume statistics (mean, std, min and max) of sub-polyhedra formed by each Voronoi facet and center atom, and independent statistics (mean, std, min, max, sum) for sub-polyhedra by i -edged facets and center atom. | 29 | | |
| $Distance_{Voro/Dist}\ stats$ | Distance statistics (mean, std, min and max) of center atom with neighbors. | 8 | | |
| Subtotal | Candidate SRO features for an atomic site. | 123 | | |

starting from the SRO feature of whether an atom is surrounded by a characteristic motif of <0,0,12,0,0> icosahedra, the generated MRO features would be sum and average number of icosahedra and std of icosahedra distribution in the neighboring shell. These features represent icosahedra connectivity in MRO, which is believed to play a role in the plastic heterogeneity of metallic glasses^{34,44}.

| Table 2 Medium-range order (MRO) feature sets generated by an automatic neighboring coarse-grained method. | | | | | |
|--|---|-------|--|--|--|
| Features | Statistical Types | Count | | | |
| $CN_{Voro/Dist} Stats_{NN}$ | mean, std, min and max of $CN_{Voro/Dist}$. | 8 | | | |
| Voronoi $idx_{37} Stats_{NN}$ | mean, std, min and max of Voronoi indices $_{37}$. | 20 | | | |
| Characteristic motifs Stats _{NN} | sum, mean, std of Characteristic motifs. | 12 | | | |
| Voronoi area/volume Stats _{NN} | mean, std, min and max of Voronoi area/volume. | 8 | | | |
| Avg. <i>i</i> -fold symm idx ₃₇ | $\sum_{m=0}^{\text{NN}} n_i^m / \sum_{m=0}^{\text{NN}} \sum_{i=3}^7 n_i^m$, where n_i denotes the number of <i>i</i> -edged facets of the Voronoi polyhedra and m iterates over each neighbor. | | | | |
| i -fold symm idx $_{37}$ Stats $_{ m NN}$ | mean, std, min and max of i -fold symm idx ₃₇ . | 20 | | | |
| Weighted i -fold symm idx ₃₇ Stats _{NN} | mean, std, min and max of Weighted i -fold symm idx ₃₇ . | 40 | | | |
| BOOP $q_{410\text{-Voro/Dist}}$ Stats _{NN} | mean, std, min and max of BOOP $q_{410\text{-Voro/Dist}}$. | 32 | | | |
| BOOP $w_{410\text{-Voro/Dist}}$ Stats _{NN} | mean, std, min and max of BOOP $w_{410\text{-Voro/Dist}}$. | 32 | | | |
| Coarse-grained BOOP $q_{4\dots10}$ - Voro/Dist | Coarse-grained ⁴⁸ lowest-order rotation-invariant \bar{q}_l ($l = 4, 6, 8$ and 10). | 8 | | | |
| Coarse-grained BOOP $w_{4\dots10}$ - Voro/Dist | Coarse-grained ⁴⁸ higher-order rotation-invariant $\overline{w_l}$ ($l = 4, 6, 8$ and 10). | 8 | | | |
| ${ m CSRO_{Voro/Dist}~Stats_{NN}}$ | mean, std, min and max of CSRO_{Voro} except for the element type. | 48 | | | |
| Facet area stats Stats _{NN} | mean, std, min and max of Facet area stats. | 116 | | | |
| Sub-polyhedra volume stats | mean, std, min and max of Sub-polyhedra volume | 116 | | | |
| $Stats_{NN}$ | stats. | 110 | | | |
| $Distance_{Voro/Dist}\ stats\ Stats_{NN}$ | mean, std, min and max of Distance _{Voro/Dist} stats. | 32 | | | |
| Structural difference | $\operatorname{mean}(F_{1\dots n}^{\operatorname{SRO}})$ - F_i^{SRO} , where F can be any possible SRO feature that has a $\operatorname{mean}_{\operatorname{NN}}$ MRO feature. | | | | |
| Subtotal | Candidate MRO features for an atomic site. | 623 | | | |

Following this neighboring coarse-grained method, we can process each specific SRO features in Table 1 to generate the MRO feature sets. Existing MRO features such as the coarse-grained BOOP⁴⁸ are also included. Table 2 summarizes the 16 MRO feature sets established in this work, totaling 623 MRO features in all.

As a summary, we create a large pool of 28 feature sets (746 features), spanning SRO and MRO, to represent the heterogeneous site environments in metallic glasses. The codes for this representation are publicly available in *amlearn* (https://github.com/Qi-max/amlearn), our recent package targeted for ML in amorphous materials, and *matminer* a comprehensive Python library for ML in materials science (https://github.com/hackingmaterials/matminer) (see Methods for more details). This representation is general and can be applied to featurize the site environments of any glass.

Importantly, our ML model will then apply aggressive feature reduction such that less than 2% of these features would actually be used in practice, in order to improve interpretability and prevent overfitting. Specifically, we eliminate low-variance (< 0.1), high-linear-correlation (> 0.99) features and use model-based feature reduction by selecting the top 50 features that are of the highest feature importances in the ML model. Finally, we perform recursive feature elimination to further reduce the total number of features used in ML to a minimal set of 13 in total (listed in Table 3).

| Table 3 The 13 features for constructing the ML models. The order is in descending order of the 5-fold cross-validation averaged feature importances. | | | | | |
|---|--|------|--|--|--|
| Rank | Feature | Rank | Feature | | |
| 1 | Facet area std | 2 | Facet area std $mean_{NN}$ | | |
| 3 | $\mathrm{Distance}_{\mathrm{Dist}} \ \mathrm{std}$ | 4 | $\mathrm{Distance_{Dist}}\ \mathrm{std}\ \mathrm{mean_{NN}}$ | | |
| 5 | $\mathrm{Distance}_{\mathrm{Voro}}$ std | 6 | $\mathrm{Distance}_{\mathrm{Voro}} \ \mathrm{min}$ | | |
| 7 | $Distance_{Voro}\ std\ mean_{NN}$ | 8 | ${\rm Zr~number_{Dist}~mean_{NN}}$ | | |
| 9 | $Distance_{Voro} \ min \ mean_{NN}$ | 10 | area-weighted 5-fold symmetry mean $_{\rm NN}$ | | |
| 11 | $\mathrm{Distance_{Dist}}\ \mathrm{min}\ \mathrm{mean_{NN}}$ | 12 | $\mathrm{Distance_{Dist}}\ \mathrm{min}\ \mathrm{min_{NN}}$ | | |
| 13 | area-weighted 5-fold symmetry | | | | |

Machine-learned "quench-in softness" for identifying plastic atoms. Using the 13 features listed in Table 3, we develop a model that predicts the susceptibility of plastic deformation of atoms based on the undeformed configuration. We use gradient boosting decision trees (GBDT) as our ML algorithm and the hyperparameters searched in this work can be found in Supplementary Table S1. The GBDT model is trained on the plastic heterogeneity data at a strain of 0.04 to learn to classify the atomic environments back in the undeformed configuration as "plastic" or "non-plastic". Due to the highly localized plasticity of glass deformation with low temperatures and slow strain rates, the plastic atoms ($\sim 4.0\% - 6.0\%$ at strain of 0.04 in different compositions and quenching rates) is heavily outnumbered by non-plastic atoms. We deal with the between-class imbalance by random equal undersampling to create a balanced dataset. We use 5-fold cross-validated area under receiver operating characteristic curve (AUC-ROC) as the scoring metric. The AUC-ROC is a scoring metric that evaluates the tradeoff between true positive rate against false positive rate as a function of chosen threshold. This metric has the advantage in that it does not depend on optimizing a specific prediction threshold and simultaneously balances the tradeoff between over- and under-predicting the number of plastic atoms. After optimizing ML models on validation set, we generalize to the glass configuration that is setaside for generalization tests. The results presented in this work are that of the generalization test on the unseen glass configuration.

Of the 3 compositions and 3 strain rates per composition studied, we begin by discussing the $Cu_{65}Zr_{35}$ metallic glass quenched under a rate of 5×10^{10} Ks⁻¹ as a first example (the other systems are discussed later). $Cu_{65}Zr_{35}$ is an optimum glass former in the Cu-Zr system, and often used as a model alloy in previous studies^{28,29,31,33–35,44}. In the ML task of using only the undeformed configuration to predict plastic atoms at a relatively large strain of 0.04, the AUC-ROC on this set-aside test glass configuration is 0.754, and the ML model captures

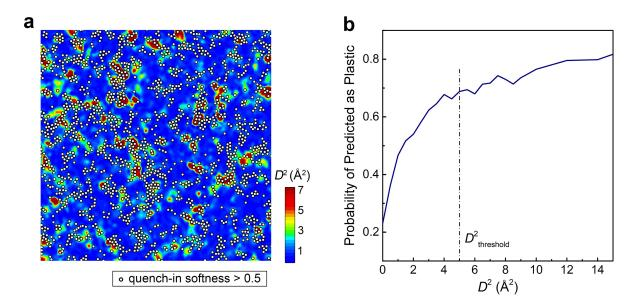


Figure 2 (color online) | Predicting plastic atoms in an optimum glass-former of $Cu_{65}Zr_{35}$ using machine learning. (a) The predicted plastic atoms (white dots) by our ML model versus the distribution of D^2 from atomistic simulations in a slice of 2.0 Å thickness at a strain of 0.04 of the prototypical glass of $Cu_{65}Zr_{35}$ quenched at a rate of 5×10^{10} Ks⁻¹. All atoms predicted with "quenchin softness" S^q larger than 0.50 are marked without prior screening. (b) The fraction of atoms within a given D^2 range that are predicted as plastic by our ML model from the underformed configuration alone. The vertical dashed line marks the D^2 threshold of 5.0 Å² that we used to classify non-plastic versus plastic atoms in this work.

73.9% of the true plastic rearrangements. This performance is comparable to previous works for predicting the step-wise plastic atoms that are activated by shear or temperature in 2-D and 3-D Lennard-Jones glasses by Cubuk et al²⁴, where the number is 73% and 72%, respectively.

Along with classification, GBDT can vote a continuous probability of each atom to be plastic, which can be considered as an indicator of the degree of plastic susceptibility. A probability of 0.50 indicates an equal possibility to be plastic or non-plastic, and the larger the probability, the greater the likelihood for the atom to be plastic. To make the probability estimates more reasonable, we further calibrate the probability estimates using isotonic regression as described previously by Zadrozny et al⁴⁹. This probabilistic plastic susceptibility is similar to the idea of "softness" defined by Cubuk et al.²⁵, except that here

the softness is absolutely determined from the initial, quenched configuration and therefore could be considered as "quench-in softness" (denoted as S^q). This atomic-scale quantity can quantitatively reflect the plastic susceptibility that is inherited from the quenched state.

We will show this ML-calibrated quench-in softness correlates strongly with the plastic atoms activated during plastic deformation. Figure 2a visualizes the atoms with S^q larger than 0.50 versus the simulated distribution of D^2 of the set-aside glass configuration at the strain of 0.04 in a slice of 2.0 Å thickness. Notably, the larger S^q atoms avoids areas of low D^2 and captures the clustering tendency of plastic atoms. Figures 2b further shows the possibility that an atom with an observed value of D^2 would be identified as plastic by the ML model. This possibility increases with the increase of D^2 , indicating that the more plastic an atom is, the more likely it is to be predicted as plastic by the ML model.

We see that our ML framework can achieve comparable success as the previous studies of Lennard-Jones glasses²⁴. However, our task is more difficult in two respects. First, we are making predictions at large strains using the undeformed configuration only, whereas the previous work used "step-by-step" training in which data from similar strains was needed for training and only small strain extrapolations were possible. Our model is unique in that, once trained, no simulations are needed to predict plastic atoms even at relatively large strains. Second, our task uses more complicated and realistic atomic interactions from the Finnis-Sinclair-type Cu-Zr EAM potentials developed by Mendelev et al.⁵⁰ versus the simpler Lennard-Jones glass used in the previous work. In addition, our model is evaluated with an external test set of glass configuration that has undergone independent quenching and deformation, and thus has different initial configuration and deformation process with the trained configurations. The ability to generalize to totally unseen glass configurations gives further evidence to the validity of our model.

Capturing the operation mechanism of plastic atoms. In practice, the fertile plastic atoms frozen in the initial configuration are activated gradually with the increase of strain. Understanding how these plastic sites operate is crucial to clarify the mechanical response of metallic glasses⁵¹. As introduced above, from the obtained ML model, we get the quenchin softness S^q as an indicator of plastic susceptibility from the site environments in the undeformed configuration. We trace the S^q distribution of plastic atoms that are activated as the strain is applied (Figure 3a, the plastic sites at typical strains are visualized in Figure 3b). We see the progression of plastic sites indeed follows a predictable sequence. At low strains, the plastic atoms correspond mainly to those predicted with high quench-in softness S^{q} , namely high probability predicted by ML to be deformable (Figure 3a). A fraction of lower S^q atoms can also be activated due to inevitable stochastic effects and shear avalanches. As the strain progresses, plasticity is induced at sites predicted with gradually lower softness according to ML (Figure 3a). This suggests a picture that the operation of plastic sites is to some degree affected by the strain or, equivalently, the applied stress. At low strains, the most unstable atoms with lower relaxation barrier could relax and contribute to plasticity, while relatively less susceptible sites are essentially frozen in their initial configuration, until the stress becomes large enough to trigger the rearrangement.

This behavior is abruptly interrupted by shear banding^{33,35,44} at a strain of ~ 0.065 (Figure 3a). Significant plastic rearrangement avalanches would occur near yielding (also see insets of Figure 3b), that is, a localized rearrangement could rapidly trigger others, leading to a cascade. Shear bands are formed, and penetrate along the shear pathway. As the atoms that form shear bands are not pre-existing structural defects, the long-lived inheritance of plastic heterogeneity on the undeformed, quenched structure is ended. Upon shear banding, plastic rearrangement abruptly extends across all levels of quench-in softness S^q (Figure 3a), suggesting that an indiscriminative transformation occurs along the pathway of shear bands.

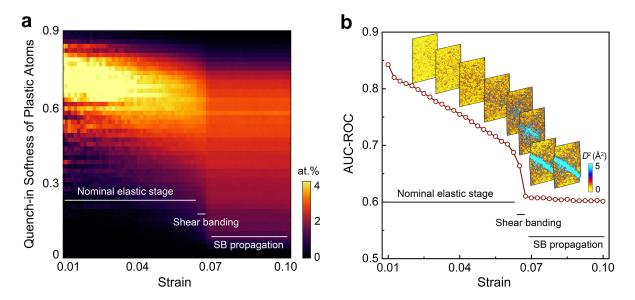


Figure 3 (color online) | Examining the qualitative nature of deformation through machine learning. (a) The distribution of quench-in softness of the plastic atoms activated under a certain strain. The entire deformation range up to the strain of 0.10 with an interval of 0.00125 is analyzed. Our ML model captures the relatively abrupt crossover between the nominal elastic stage (high correspondence between ML prediction and plastic atoms) and the shear banding and shear band propagation stages (plastic rearrangement extending across all levels of quench-in softness). (b) The AUC-ROC (area under receiver operating characteristic curve) calculated by analyzing the true positive rate and false positive rate for each strain up to 0.10. The plastic atoms at the strain from 0.02 to 0.08 with an interval of 0.01 as well as 0.065 are shown as cyan-blue atoms in the insets.

This penetrating transformation releases the stresses, causing the glass to yield. Afterwards, the S^q distribution of plastic atoms is almost uniform, due to the localized strain on already deformed atoms within shear bands (Figure 3a). Interestingly, these stage characteristics and crossovers can be revealed and supported by ML, as marked by the stages in Figure 3a.

Presenting these conclusions in a slightly different manner, we analyze and show the accuracy of our ML-calibrated quench-in softness in determining the operated plastic sites up to each strain (as denoted by the AUC-ROC) in Figure 3b. During the elastic stage, the prediction score gradually decreases yet still retains a high level (larger than 0.70), and as shown in the previous section, the model has a good predictability at a relatively large strain of 0.04. Afterwards, upon the formation of shear bands, the ML accuracy score abruptly drops. This is overall in accord with the scenarios revealed in Figure 3a. Here the ML score

actually serves as a reflection of the underlying physics of deformation, delineating the crossover of strain region dominated by localized quench-in defects and that forming shear bands by percolation. With reasonable design, ML could help track the dynamical evolution and gain insights on the underlying physics of material responses.

Effect of composition and quenching rate. In previous sections, we focused on the $Cu_{65}Zr_{35}$ glass under a quenching rate of 5×10^{10} Ks⁻¹. We next examine different compositions and thermal histories as these factors are known to affect deformation behavior¹⁶. We first discuss the effect of thermal history. Figure 4a shows the AUC-ROCs for the $Cu_{65}Zr_{35}$ glasses quenched under faster rates of 5×10^{11} Ks⁻¹ and 5×10^{12} Ks⁻¹. As expected, we see that the prediction scores as these fast-quenched glasses are relatively lower than that of the $Cu_{65}Zr_{35}$ glass with slower rate (dotted line in Figure 4a). From a viewpoint of potential energy landscape (PEL), the path lengths between neighboring minima on the PEL are shorter in a rapidly quenched system than in a more relaxed system¹¹, yielding a much higher density of local PEL minima in the rapidly quenched glasses⁵². This could make fast-quenched glasses more susceptible to cascades, and the enhanced non-local activation lowers the inheritance of plastic rearrangement on the undeformed structure itself. This is consistent with recent experiments⁵³ which demonstrated the density of plastic regions and cascades is significantly higher in a less relaxed system compared with a better annealed system.

Next, we examine the effect of changing composition. We take the $Cu_{80}Zr_{20}$ @ 5 × 10¹⁰ Ks⁻¹ and $Cu_{50}Zr_{50}$ @ 5 × 10¹⁰ Ks⁻¹ glass systems as examples (Figure 4a). We see the prediction scores of $Cu_{80}Zr_{20}$ are comparable to and even slightly higher than those of $Cu_{65}Zr_{35}$, while the scores of $Cu_{50}Zr_{50}$ are lower than $Cu_{65}Zr_{35}$. Interestingly, many experiment and simulation studies observed that $Cu_{50}Zr_{50}$ does have a lower plastic heterogeneity than

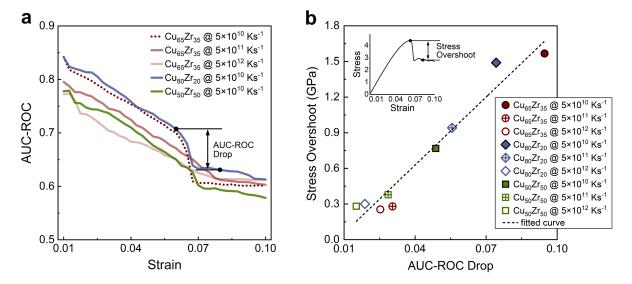


Figure 4 (color online) | Composition and quenching history tuning the predictabilities of plastic atoms. (a) The AUC-ROCs calculated with evolving strains for 4 prototypical glasses, i.e., $Cu_{65}Zr_{35}$ @ 5×10^{11} Ks⁻¹ and $Cu_{65}Zr_{35}$ @ 5×10^{12} Ks⁻¹ as well as $Cu_{80}Zr_{20}$ @ 5×10^{10} Ks⁻¹ and $Cu_{50}Zr_{50}$ @ 5×10^{10} Ks⁻¹ with different thermal histories or compositions. The AUC-ROC of the $Cu_{65}Zr_{35}$ @ 5×10^{10} Ks⁻¹ glass (as extracted from Figure 3b) is represented by a red dotted line for comparison. (b) Link between the ML-benchmarked structural disordering upon shear banding with the corresponding stress overshoot (as illustrated in the inset) extracted from the stress-strain curves in deformation simulations. The dashed line shows the fitted curve ($R^2 = 0.94$).

 $Cu_{65}Zr_{35}^{29,31,34}$. As proof, we analyze the standard deviation of quench-in softness, $\sigma_S = \sqrt{\langle S^2 \rangle - \langle S \rangle^2}$, for the atoms in the 3 glasses, and σ_S for $Cu_{50}Zr_{50}$, $Cu_{65}Zr_{35}$ and $Cu_{80}Zr_{20}$ @ 5×10^{10} Ks⁻¹ are 0.177, 0.216 and 0.223, respectively. σ_S essentially evaluates the internal contrast of plastic susceptibility and is lowest in $Cu_{50}Zr_{50}$ of the 3 glasses, thus providing atomic-level evidence to the experiment and simulation observations.

Another noteworthy point is that the degree of prediction score drop upon yielding is remarkably different among the glasses (Figure 4a). As mentioned previously, the ML score drop is result of the indiscriminative and penetrating deformation accompanied by shear banding. We see the increase of quenching rates reduces the degree of score drop, and $Cu_{80}Zr_{20}$ or $Cu_{65}Zr_{35}$ glasses have sharper drop than that of $Cu_{50}Zr_{50}$ (Figure 4a). In another aspect, the stress overshoot $(\Delta\sigma)$ upon yielding^{29,34,54} is believed to be a measurable

indication of shear localization degree of a glass (see Figure 4b inset for an illustration). We then extract the stress overshoot $\Delta \sigma$ from the strain of 0.06 (roughly corresponding to the largest stress, or say strength) to 0.08 (after shear band matures) from the stress-strain curves of all 9 model glasses (see Supplementary Figure S3) and the corresponding AUC-ROC drop in Figure 4b. Interestingly, evident positive correlation can be drawn, indicating a linkage between these two parameters: the degree of accuracy drop in the ML model is a reflection of penetrating deformation upon shear banding and correlated with the stress overshoot in the sample.

3. Discussion

Generalization across different compositions and quench rates. Thus far, we have trained our ML model for a certain glass system and tested on unseen glass configurations under the same conditions (i.e., same composition and quench rate). This are already rigorous generalization tests that beyond the traditional train-to-test within a single dataset. Such tests give us confidence on the validity of our ML models. Going even further, there are another more challenging yet significant question of whether our ML models can generalize between different thermal histories and compositions, i.e., whether a model trained under one condition can accurately make predictions under different conditions. These tests are indeed to make predictions on occasions that are far beyond the bounds of what is encompassed in the training data. This kind of generalization tests have not been done in previous glass studies^{24,25} and are indeed challenging for all kinds of ML studies.

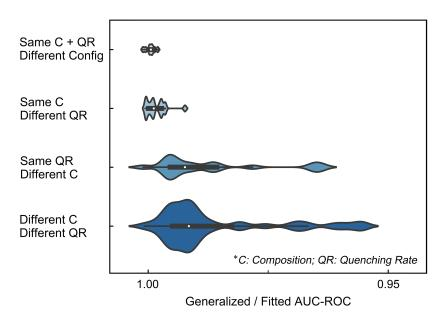


Figure 5 (color online) | Generalizability of machine learning models to unseen glasses with different compositions and quench rates. Violin plots of the generalization performances of our ML models on 4 generalization scenarios: i) same composition (abbreviated as C) and same quenching rate (QR) but to new unseen configurations, ii) same composition and different quenching rate; iii) different composition and same quenching rate; iv) different composition and different quenching rate. The performance is evaluated by dividing the generalization score by the original, same-condition score; all generalization scores achieve more 95% of the same-condition scores. The height of the violin plot indicates the number of tests that fall within a performance interval and the interior shows the box plots.

To resolve this unsettled issue, we have tested all 81 possible mutual generalization pairs between the 9 glasses with different compositions and quenching rates. The tests are generally grouped into 3 categories: i) between glasses with same composition but different quenching rate (18 tests are within this category); ii) same quenching rate but different composition (18 tests); and iii) different composition and different quenching rate (45 tests). We also include the generalization to unseen glass configurations with same composition and same quenching rate for comparison (9 tests). The generalization performance is evaluated by dividing the generalization score by the score when testing the model for the same conditions (i.e., the fraction of the original score retained upon generalization). Figure 5 plots the generalization performances for the 4 generalization categories. We demonstrate

that the generalized scores overall achieve more 95% of the same-condition scores, indicating a strong generalizability between glasses. This shows that our ML models do capture the traits of plastic atoms in Cu-Zr metallic glasses and interestingly, these learnt structural traits are largely common to glasses with various compositions and thermal histories. Practically speaking, it indicates that an ML model trained using simulations on one system can be confidently re-applied to other systems without performing additional simulations.

Interpreting the machine learning model. We demonstrate that our ML model predicts an atomic-scale quantity, quench-in softness, as an indication of plastic susceptibility of atoms, from the quenched configuration alone, and is robust and readily generalizable across glasses and quenching conditions. To understand how ML achieves such success, it is interesting to look closer into how the ML models makes decisions based on the feature space.

Due to the difficulty of directly visualizing the decision boundary in high-dimensional feature space, partial dependence plots (PDP) offers a mechanism for interpreting the ML model⁵⁵. PDP resolves the effect of specific features by marginalizing the model output over other features, in essence measuring how the model prediction changes as a function of the target features. Often 1 or 2 features are selected in a time, generating 1-dimensional (1-D) and 2-dimensional (2-D) PDP plots. A positive partial dependence indicates that plastic probability increases in that feature range and vice versa.

Figure 6a plots the 2-D PDP of the top-6 ranked features in Table 3. We see that the ML model tends to predict the atoms as plastic when their neighbors form anisotropic environments with a large standard deviation in their facet areas or bond lengths. This effect is more pronounced when such anisotropy is present at both the short- and medium-ranges. As another signature, atoms with small minimum bond lengths in the nearest-neighbor shell (SRO distance_{Voro} min), are more prone to deform. This is reasonable as when

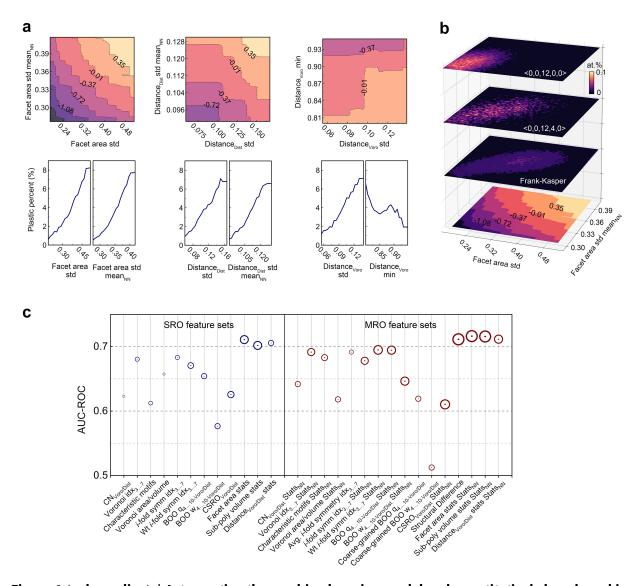


Figure 6 (color online) | Interpreting the machine learning model and quantitatively benchmarking the predictive power of each individual short- or medium-range order feature set. (a) Two-dimensional (2-D) partial dependence plots (PDPs) of the top 6 features of the ML model. The plastic atom percent with varying features are also analyzed from the deformation data and match the PDPs. (b) Projecting <0,0,12,0,0>, <0,0,12,4,0> and Frank-Kasper clusters to 2-D PDP of top-2 features of the ML model to interpret the origin of stability of these characteristic motifs long proposed for metallic glasses; conventional descriptors only capture a small fraction of the possible input space. (c) Quantitatively benchmarked predictive powers of individual SRO (left panel) and MRO (right panel) feature sets. We iteratively feed each individual feature set to train a ML model and use the resultant AUC-ROC as the metric for their predictive power. The sphere size is proportional to the number of features within each feature set.

the atoms are closer than their equilibrium distance, the repulsive force dominates and tends to propel the atoms to move. The lower panel in Figure 6a shows the percent of plastic atoms in the data set (independent of any ML model) when varying these features, showing that the ML model is indeed picking up on realistic correlations (and their combinations) hidden in the data. These scenarios can serve as simple heuristic rules in locating the plastic units in metallic glasses. In addition, the other 7 features listed in Table 3 also contribute to the prediction together with these 6 features, in a collective way. The collective use of many features made possible by the ML approach is in contrast to the typical approach in which predictions of plastic atoms are made based on essentially only one signature.

Understanding the stability of long-proposed characteristic motifs. In previous studies, researchers often use icosahedra (with a Voronoi index of <0,0,12,0,0>, or <0,0,12,0> if omitting facets with 7 edges and more), <0,0,12,4,0> or Frank-Kasper clusters³⁷ (or referred to as "Z clusters" by Chen et al⁹) as characteristic motifs in metallic glasses^{29,31,34}. Interestingly, some traits of these motifs, such as a large degree of local 5-fold symmetry, have been verified by the ultrahigh resolution nanobeam electron diffraction experiments⁵⁶. In this study, these characteristic motifs are tested as part of the SRO representation (Table 1). However, they are found to contribute little to the actual decision-making process and removed during the feature elimination process, and thus unused in the final ML models. This could be attributed to two factors: i) these categorical features are highly degenerate, limiting their distinguishability of the heterogeneous environments. ii) the message carried by these characteristic motifs could already be represented by other features chosen by ML.

To test this, we plot the 2D feature space corresponding to our top 2 features and overlay the positions in that space for sites corresponding to <0,0,12,0,0> icosahedra, <0,0,12,4,0> and Frank-Kasper clusters (Figure 6b). Icosahedra are regular polyhedra with

all five-edged facets and naturally features low deviations in facet areas or bond lengths. We see that sites corresponding to the icosahedra <0,0,12,0,0> are densely clustered in the low facet area deviation corner of the PDP plot, which is exactly the region that corresponds to low plastic susceptibility. <0,0,12,4,0> and Frank-Kasper clusters distribute more dispersively, yet still largely within the low plastic susceptibility regions. This interprets the observed stability of these long-proposed characteristic motifs. Nonetheless, all these characteristic motifs are generally distributed only in a narrow portion of the entire feature space, roughly along the direction in which the facet area variations are proportional for the nearest and second-nearest neighbors. In contrast, our top 2 ML features form a more complete description of feature space (Figure 6b). These features capture not only the stable nature of regions of feature space corresponding to these characteristic motifs, but also the effect of other and less conventional feature combinations (e.g., irregular arrangement of near neighbors but regular arrangement of second-nearest neighbors) to form the final decision boundary.

Quantitatively evaluating the existing/proposed signatures. As described previously, we construct a large representation that spans SRO (Table 1) and MRO (Table 2) in metallic glasses and is composed of 28 feature sets and 740+ total features as candidates for constructing the ML model. Later, we regressively reduce the representation to 13 features (Table 3) to get the simplest model that interprets the data, and these 13 features form a reasonable feature space for distinguishing the plastic atoms. However, the individual predictive ability of the 28 SRO or MRO feature sets are largely buried. To re-examine the predictability of each feature set (independent of the presence of other features), we iteratively feed each individual feature set alone to train a ML model, and use the resultant AUC-ROC on distinguishing the plastic atoms as a metric of that feature set's predictive

capability (Figure 6c).

From Figure 6c, we see that Voronoi facet area statistics achieve highest prediction ability in all SRO and MRO feature sets, achieving scores of ~0.710. Voronoi sub-polyhedra volume statistics and distance statistics are also among the best ones in identifying plastic atoms. These feature sets are new feature sets introduced in this work, and could be reapplied to other glass characterization problems in the future. As to the existing recognized SRO features, we see that the SRO Characteristic motifs features achieves a relatively low prediction score of 0.612; similar results are present for $\text{CN}_{\text{Dist/Voro}}$ with a score of 0.623. The Voronoi area/volume and bond-order-related BOOP q_{4-10}^{40} have slightly higher scores of 0.650, while the higher-order BOOP w_{4-10}^{40} has the lowest score of 0.576 among SRO sets. CSRO-related features^{46,47} are also found to be not very useful for predicting plastic heterogeneity in metallic glasses such as $\text{Cu}_{65}\text{Zr}_{35}$ where composition segregation is not so pronounced. Voronoi indices and the derived i-fold symmetry indices³⁹ have the highest scores of ~0.680 among the historically used SRO features.

Interestingly, almost all MRO feature sets outperform their corresponding SRO sets (Figure 6c), indicating that plastic heterogeneity does correlate with a larger structural length scale beyond nearest-neighbors. For example, when extended to MRO, the predictive power of the characteristic motifs features has greatly enhanced, reaching an AUC-ROC of 0.683 (compared to 0.612 of SRO). This evidences that the cluster-cluster connection of these characteristic motifs in the medium-range are indeed important, as discussed in some previous studies^{31,34,44}. As an exception, the predictive power of CSRO features is slightly decreased from SRO 0.626 to MRO 0.610, suggesting that the chemical inhomogeneity is less pronounced at a larger length scale. We believe the general strategy for transforming existing SRO descriptors into MRO descriptors is an additional contribution that may be relevant to many future problems.

We have interpreted the dependence of deformation probability on the features of each of the 28 SRO or MRO feature sets by analyzing the PDPs for various feature combinations (see Supplementary Figures S4 - S31). As the discussion regarding the best site descriptors for application to metallic glass continues, we believe ML can help establish a more complete, quantitative picture for evaluating the relations between structural signatures and plastic heterogeneity.

Possible benefits to designing metallic glasses with desired property. In addition to helping us to understand the structure-deformation relationship, extensions of our ML model may ultimately help in designing metallic glasses with desired deformation behaviors. Our findings demonstrate that much of plasticity within the elastic regime is controlled by the quench-in softness that is determinant by the initial glass configuration, rather than complex dynamics. Thus, any route that can modify the inherent structure would have a chance to tailor the density or distribution of plastic units and thus tailor the resultant deformation responses. For instance, it has long been proposed that to make metallic glasses ductile, a larger density of plastic units is preferred, and plausible routes can be changing the thermal history, such as ultrafast quenching, rejuvenating glass structure through thermomechanical cycling, or applying irradiation techniques to transform the glass into more deformable structural state¹⁶. Relying on experiments, even deformation simulations to test the possible ideas could be rather time-consuming (a 5×10^7 s⁻¹ deformation of large simulation cells such as those containing $\sim 3 \times 10^5$ atoms in this work can take ~ 5000 CPU hours). The use of ML as demonstrated in this work could greatly accelerate the development cycle of glasses with targeted mechanical behaviors. In addition to deformation, our ML framework is indeed general and readily generalizable to the studies of other site properties and may also be applied to important processes such as glass transition, thermal activation, and relaxation.

Methods

Liquid Quenching and Compressive Simulation. We simulate quenching and deformation of a series of Cu-Zr metallic glasses using molecular dynamics simulations. A total of 9 model glasses, with 3 varying compositions of Cu_zZr_{1-x} (x=50,65 and 80 at.%), and 3 liquid melt quenching rates of 5×10^{10} , 5×10^{11} and 5×10^{12} Ks⁻¹ are used. For each model glass, we construct 3 large slab samples, each of which containing 345600 atoms with dimensions ~120 (X) × 24 (Y) ×240 (Z) Å³. Data from 2 glass samples are concatenated and split into training and validation sets for training the ML models, while another 1 sample is set-aside for rigorous generalization tests. During simulations, initial configurations of the samples are built by random substituting Zr in Cu fcc crystal lattice. These models are annealed at 2000 K for 1 ns, quenched to 50 K with one of the 3 quenching rates, respectively, and finally relaxed at 50 K for 1 ns. We use LAMMPS package⁵⁷ and Finnis-Sinclair-type Cu-Zr EAM potentials developed by Mendelev et al. ⁵⁰ The timestep is set as 1 fs. Temperature and pressure are controlled by Nosé-Hoover thermostat and barostat.

After quenching, the Cu-Zr glass samples are compressed along Z axis under a strain rate of 2.5×10^7 s⁻¹ in a quasi-static mode. Compression is carried out at a low temperature of 50 K to pronounce the heterogeneous deformation. Periodic boundary conditions are imposed in Y and Z axes and free surfaces are applied along X axis to allow shear offsets. This simulation scheme has been previously demonstrated to be reasonable in revealing the heterogeneous deformation in metallic glasses^{29,31,34}. In constructing the ML datasets, we select atoms within dimensions ~100 $(X) \times 24$ $(Y) \times 200$ (Z) Å³ to avoid effects of free surfaces and two ends of the compressive direction.

It is worth noting that the strategy of quenching a small cell and replicating it to build a large simulation cell for deformation simulation does not work in this study. This strategy is used in many glass deformation papers^{29,31,34}, helping save a large amount of simulation

time, and seems to have no significant effects on the deformation behaviors. However, in generating data for ML, this would generate replicated site environments that are of no help, even harmful for subsequent ML in that it can lead to overfitting and overestimation of the generalization score. In this work, we have simulated un-replicated, large enough samples to guarantee the variety of site environments for ML.

Plastic Heterogeneity Analyses. In contrast to the dislocation-mediated mechanism in crystals, the deformation in metallic glasses is largely heterogeneous and difficult to discern. Effective mechanical indicators are needed to detect plastic events in metallic glasses. In this work, we employ non-affine displacement (D^2) as the plastic indicator¹⁴. To calculate D^2 , the locally affine transformation matrix, J_i , that best maps $\{d^0_{ji}\} \rightarrow \{d_{ji}\}$, $\forall j \in N^0_i$, is obtained by minimizing $\sum_{j \in N^0_i} \left| d^0_{ji} J_i - d_{ji} \right|^2$,

$$J_{i} = \left(\sum_{j \in N_{i}^{0}} d_{ji}^{0T} d_{ji}^{0}\right)^{-1} \left(\sum_{j \in N_{i}^{0}} d_{ji}^{0T} d_{ji}\right)$$
(2)

where d_{ji} and d_{ji}^0 are the vector separation (row vectors) between atom j and i and superscript 0 indicates the reference configuration. Here, j is one of atom i's nearest neighbors, and N_i^0 is the total number of nearest-neighbors of atom i at the reference configuration. Next, the Lagrangian strain matrix is computed as:

$$\eta_i = \frac{1}{2} \left(J_i J_i^T - I \right) \tag{3}$$

Finally, the D^2 for atom i can be defined as:

$$D_i^2 = \frac{1}{N} \sum_j [\vec{r}_j(t) - \vec{r}_i(t) - J_i(\vec{r}_j(t - \Delta t) - \vec{r}_i(t - \Delta t))]^2$$
 (4)

Here D^2 is calculated based on a slightly modified code from OVITO⁵⁸. The cutoff in calculating D^2 is set to be 4.5 Å, which falls roughly between the 1st and 2nd peaks in the pair correlation functions of the Cu-Zr glasses. By setting a D^2 threshold of 5.0 Å², we can indicate whether an atom is plastic or not at a typical strain such as 4.0%.

Site Environments Representation of Metallic Glasses. In previous studies, researchers often use SRO and MRO to describe the atomic packing in metallic glasses; each is divided into geometric (often referred to as "topological") and chemical order⁹. We choose to follow these conventions in categorizing features. For geometric SRO, we first featurize coordination number (CN)³⁶, Voronoi indices³⁶, characteristic motifs^{37,38}, *i*-fold symmetry indices³⁹ and bond-orientational order parameters (BOOP)⁴⁰, which are among the most recognized structural signatures in the field of metallic glasses. The range of Voronoi indices and the ifold symmetry indices is from 3 to 7, representing the 3- to 7-fold symmetry in local environments. We also use Voronoi facet areas to derive the weighted i-fold symmetry indices. Whether each atom belongs to the characteristic motifs e.g. <0.0,12,0.0> icosahedra, <0,0,12,4,0> or Kasper-type clusters³⁷ is featurized by one-hot encoding. The distances, areas and volumes are mean-normalized to be comparable among different systems. For chemical SRO, we featurize the element type, the number and fraction of each element in the neighboring shell and Warren-Cowley parameters that denotes deviation of local chemistry with nominal composition^{46,47}. Voronoi tessellation (signified by subscript "Voro" e.g. CN_{Voro}) and cutoff distance (subscript "Dist" e.g. CN_{Dist}) are both used to define neighbors when calculating CN, BOOP, distance statistics and CSRO. In addition, we introduce new features as explained in the main text. A more detailed summary of the 12 SRO feature sets is listed in Table 1. Details of the MRO representation scheme is presented in the main text and in Table 2.

The site representation in this work are derived using a set of Fortran and Python codes written by the authors. The codes can be publicly accessed in our open-source package targeted for ML for amorphous materials, *amlearn*, and a comprehensive open-source Python library for ML in materials science, *matminer*¹⁸. In *amlearn*, we wrap Fortran 90 subroutines and functions with Python using f2py⁵⁹ to combine usability and fast-

computation (>10x times faster than pure Python). The computation efficiency is particularly important for large atom systems, e.g. metallic glass samples constructed in this work with several hundreds of thousands of atoms. The official websites of amlearn and matminer are https://github.com/Qi-max/amlearn and https://github.com/hackingmaterials/matminer.

References

- 1. Angell, C. A. Formation of Glasses from Liquids and Biopolymers. *Science* **267**, 1924–1935 (1995).
- 2. Hiemenz, P. C. & Hiemenz, P. C. Principles of colloid and surface chemistry. *New York: M. Dekker* (1986).
- 3. Jaeger, H. M., Nagel, S. R. & Behringer, R. P. Granular solids, liquids, and gases. Rev. Mod. Phys. 68, 1259–1273 (1996).
- 4. Pusey, P. N. & Van Megen, W. Phase behaviour of concentrated suspensions of nearly hard colloidal spheres. *Nature* **320**, 340–342 (1986).
- 5. Carlson, D. E. & Wronski, C. R. Amorphous silicon Solar Cells. *Appl. Phys. Lett.* **28**, 671-673 (1976).
- 6. Klement, W., Willens, R. H. & Duwez, P. Non-crystalline structure in solidified Gold-Silicon alloys. *Nature* **187**, 869–870 (1960).
- Johnson, W. L. Bulk glass-forming metallic alloys: science and technology. MRS Bull.
 24, 42-56 (1999).
- 8. Wang, W. H., Dong, C. & Shek, C. H. Bulk metallic glasses. *Mater. Sci. Eng. R: Rep.* **44,** 45–90 (2004).
- 9. Cheng, Y. Q. & Ma, E. Atomic-level structure and structure-property relationship in metallic glasses. *Prog. Mater. Sci.* **56**, 379–473 (2011).
- Trexler, M. M. & Thadhani, N. N. Mechanical properties of bulk metallic glasses.
 Prog. Mater. Sci. 55, 759–839 (2010).
- 11. Fan, Y., Iwashita, T. & Egami, T. How thermally activated deformation starts in metallic glass. *Nat. Commun.* **5**, 5083 (2014).
- 12. Greer, A. L., Cheng, Y. Q. & Ma, E. Shear bands in metallic glasses. *Mater. Sci. Eng. R: Rep.* **74**, 71–132 (2013).

- 13. Argon, A. S. Plastic deformation in metallic glasses. *Acta Met.* 27, 47–58 (1979).
- Falk, M. L. & Langer, J. S. Dynamics of viscoplastic deformation in amorphous solids.
 Phys. Rev. E Stat. Physics, Plasmas, Fluids, Relat. Interdiscip. Top. 57, 7192–7205 (1998).
- Pan, D., Inoue, A., Sakurai, T. & Chen, M. W. Experimental characterization of shear transformation zones for plastic flow of bulk metallic glasses. *Proc. Natl. Acad.* Sci. 105, 14769-14772 (2008).
- 16. Ma, E. & Ding, J. Tailoring structural inhomogeneities in metallic glasses to enable tensile ductility at room temperature. *Mater. Today* **19**, 568-579 (2016).
- 17. Greer, A. L. Metallic glasses...on the threshold. *Mater. Today* 12, 14-22 (2009).
- 18. Ward, L. et al. Matminer: An open source toolkit for materials data mining. Comput.

 Mater. Sci. 152, 60-69 (2018).
- 19. Ren, F. *et al.* Accelerated discovery of metallic glasses through iteration of machine learning and high-throughput experiments. *Sci. Adv.* 4, eaaq1566 (2018).
- 20. Botu, V., Batra, R., Chapman, J. & Ramprasad, R. Machine learning force fields: Construction, validation, and outlook. *J. Phys. Chem. C* **121**, 511–522 (2017).
- 21. Gossett, E. et al. AFLOW-ML: A RESTful API for machine-learning predictions of materials properties. Comput. Mater. Sci. 152, 134-145 (2018).
- 22. Ward, L., Agrawal, A., Choudhary, A. & Wolverton, C. A General-Purpose Machine Learning Framework for Predicting Properties of Inorganic Materials. npj Comput. Mater. 2, 16028 (2016).
- Bartók, A. P., Payne, M. C., Kondor, R. & Csányi, G. Gaussian approximation potentials: The accuracy of quantum mechanics, without the electrons. *Phys. Rev.* Lett. 104, 136403 (2010).
- 24. Cubuk, E. D. et al. Identifying structural flow defects in disordered solids using

- machine-learning methods. Phys. Rev. Lett. 114, 108001 (2015).
- 25. Cubuk, E. D. *et al.* Structure-property relationships from universal signatures of plasticity in disordered solids. *Science*. **358**, 1033–1037 (2017).
- 26. Daw, M. S., Foiles, S. M. & Baskes, M. I. The embedded-atom method: a review of theory and applications. *Mater. Sci. Rep.* **9**, 251-310 (1993).
- 27. Tang, M. B., Zhao, D. Q., Pan, M. X. & Wang, W. H. Binary Cu-Zr bulk metallic glasses. *Chinese Phys. Lett.* **21**, 901 (2004).
- 28. Ding, J., Patinet, S., Falk, M. L., Cheng, Y. & Ma, E. Soft spots and their structural signature in a metallic glass. *Proc. Natl. Acad. Sci.* **111**, 14052-14056 (2014).
- 29. Cao, A. J., Cheng, Y. Q. & Ma, E. Structural processes that initiate shear localization in metallic glass. *Acta Mater.* **57**, 5146–5155 (2009).
- 30. Cheng, Y. Q. & Ma, E. Atomic-level structure and structure-property relationship in metallic glasses. *Prog. Mater. Sci.* **56**, 379-473 (2011).
- 31. Li, M., Wang, C. Z., Hao, S. G., Kramer, M. J. & Ho, K. M. Structural heterogeneity and medium-range order in Zr_xCu_{100-x} metallic glasses. *Phys. Rev. B* **80**, 184201 (2009).
- 32. Chen, H. et al. Carbonophosphates: A New Family of Cathode Materials for Li-Ion Batteries Identified Computationally. Chem. Mater. 24, 2009–2016 (2012).
- 33. Wang, X. D. et al. Atomic Structure of Binary Cu_{64.5}Zr_{35.5} Bulk Metallic Glass. Appl. Phys. Lett. **92**, 011902 (2008).
- 34. Lee, M., Lee, C. M., Lee, K. R., Ma, E. & Lee, J. C. Networked interpenetrating connections of icosahedra: Effects on shear transformations in metallic glass. *Acta Mater.* **59**, 159–170 (2011).
- 35. Xu, D., Lohwongwatana, B., Duan, G., Johnson, W. L. & Garland, C. Bulk metallic glass formation in binary Cu-rich alloy series $Cu_{100-x}Zr_x$ (x = 34, 36, 38.2, 40 at.%) and mechanical properties of bulk $Cu_{64}Zr_{36}$ glass. *Acta Mater.* **52**, 2621-2624 (2004).

- 36. Okabe, A., Boots, B., Sugihara, K. & Chiu, S. N. Spatial Tesselations. Concepts and Applications of Voronoi Diagrams (2009).
- 37. Frank, F. C. & Kasper, J. S. Complex alloy structures regarded as sphere packings.I. Definitions and basic principles. Acta Crystallogr. 11, 184–190 (1958).
- 38. Sheng, H. W., Luo, W. K., Alamgir, F. M., Bai, J. M. & Ma, E. Atomic packing and short-to-medium-range order in metallic glasses. *Nature* **439**, 419–425 (2006).
- 39. Peng, H. L., Li, M. Z. & Wang, W. H. Structural signature of plastic deformation in metallic glasses. *Phys. Rev. Lett.* **106**, 135503 (2011).
- 40. Steinhardt, P. J., Nelson, D. R. & Ronchetti, M. Bond-orientational order in liquids and glasses. *Phys. Rev. B* **28**, 784–805 (1983).
- Widmer-Cooper, A., Perry, H., Harrowell, P. & Reichman, D. R. Irreversible reorganization in a supercooled liquid originates from localized soft modes. *Nat. Phys.* 4, 711–715 (2008).
- 42. Manning, M. L. & Liu, A. J. Vibrational modes identify soft spots in a sheared disordered packing. *Phys. Rev. Lett.* **107**, 180302 (2011).
- 43. Ding, J. et al. Universal structural parameter to quantitatively predict metallic glass properties. Nat. Commun. 7, 13733 (2016).
- 44. Cowley, J. M. An approximate theory of order in alloys. *Phys. Rev.* **77**, 669–675 (1950).
- 45. Warren, B. E. X-ray diffraction. Analysis 1, 402 (1990).
- 46. Krizhevsky, A., Sutskever, I. & Hinton, G. E. 1 ImageNet Classification with Deep Convolutional Neural Networks. Adv. Neural Inf. Process. Syst. (2012).
- 47. Soklaski, R., Nussinov, Z., Markow, Z., Kelton, K. F. & Yang, L. Connectivity of icosahedral network and a dramatically growing static length scale in Cu-Zr binary metallic glasses. *Phys. Rev. B* 87, 184203 (2013).

- 48. Lechner, W. & Dellago, C. Accurate determination of crystal structures based on averaged local bond order parameters. *J. Chem. Phys.* **129**, 114707 (2008).
- 49. Zadrozny, B. & Elkan, C. Obtaining calibrated probability estimates from decision trees and naive Bayesian classifiers. in *Proceedings of the 18th International Conference on Machine Learning* (2001).
- 50. Mendelev, M. I., Rehbein, D. K., Ott, R. T., Kramer, M. J. & Sordelet, D. J. Computer simulation and experimental study of elastic properties of amorphous Cu-Zr alloys. J. Appl. Phys. 102, 093518 (2007).
- 51. Hufnagel, T. C., Schuh, C. A. & Falk, M. L. Deformation of metallic glasses: Recent developments in theory, simulations, and experiments. *Acta Mater.* **109**, 375-393 (2016).
- 52. Stillinger, F. H. A Topographic View of Supercooled Liquids and Glass Formation.

 Science 267, 1935–1939 (1995).
- 53. Li, W., Bei, H., Tong, Y., Dmowski, W. & Gao, Y. F. Structural heterogeneity induced plasticity in bulk metallic glasses: From well-relaxed fragile glass to metallike behavior. *Appl. Phys. Lett.* **17**, 171910 (2013).
- 54. Wang, Q., Li, J. H., Liu, J. B. & Liu, B. X. Structural skeleton of preferentially interpenetrated clusters and correlation with shear localization in Mg-Cu-Ni ternary metallic glasses. *Phys. Chem. Chem. Phys.* **16**, 19590-19601 (2014).
- 55. Friedman, J. H. Greedy function approximation: A gradient boosting machine. *Ann. Stat.* 1189-1232 (2001).
- 56. Hirata, A. et al. Direct observation of local atomic order in a metallic glass. Nat. Mater. 10, 28–33 (2011).
- 57. Plimpton, S. Fast parallel algorithms for short-range molecular dynamics. *J. Comput. Phys.* **117**, 1–19 (1995).

- 58. Stukowski, A. Visualization and analysis of atomistic simulation data with OVITO-the Open Visualization Tool. *Model. Simul. Mater. Sci. Eng.* **18**, 015012 (2010).
- 59. Peterson, P. F2PY: a tool for connecting Fortran and Python programs. *Int. J. Comput. Sci. Eng.* **4**, 296-305 (2009).

Code and Data availability

The featurization and ML codes can be publicly found in our open-source packages amlearn https://github.com/Qi-max/amlearn and matminer https://github.com/hackingmaterials/matminer. The datasets used in this work are available in https://figshare.com/articles/Plastic_Heterogeneity_Data_of_Cu-Zr_Metallic_Glasses/7941014

Acknowledgements

QW and AJ acknowledge support from U.S. Department of Energy, Office of Basic Energy Sciences, Early Career Research Program, which intellectually led the effort. QW acknowledges the support of National Natural Science Foundation of China (51701190). This research used resources of the National Energy Research Scientific Computing Center (NERSC), a U.S. Department of Energy Office of Science User Facility operated under Contract No. DE-AC02-05CH11231, and the National Supercomputing Center in Shenzhen, China.

Authors' information

QW and AJ developed the plan for this study. QW performed the simulations and developed the machine learning models. QW and AJ analyzed the results and wrote the manuscript. Correspondence and requests for materials should be addressed to QW (qwang3@lbl.gov) and AJ (ajain@lbl.gov).

Competing interests

The authors declare no competing interests.